

Extending the coherence of a quantum dot hybrid qubit

Brandur Thorgrimsson,¹ Dohun Kim,² Yuan-Chi Yang,¹ L. W. Smith,¹ C. B. Simmons,¹ Daniel R. Ward,^{1,*} Ryan H. Foote,¹ J. Corrigan,¹ D. E. Savage,³ M. G. Lagally,³ Mark Friesen,¹ S. N. Coppersmith,¹ and M. A. Eriksson¹

¹*Department of Physics, University of Wisconsin-Madison, Madison, WI 53706, USA*

²*Department of Physics and Astronomy, Seoul National University, Seoul 08826, South Korea*

³*Department of Materials Science and Engineering,
University of Wisconsin-Madison, Madison, WI 53706, USA*

Identifying and ameliorating dominant sources of decoherence are important steps in understanding and improving quantum systems. Here we show that the free induction decay time (T_2^*) and the Rabi decay rate (Γ_{Rabi}) of the quantum dot hybrid qubit can be increased by more than an order of magnitude by appropriate tuning of the qubit parameters and operating points. By operating in the spin-like regime of this qubit, and choosing parameters that increase the qubit's resilience to charge noise (which we show is presently the limiting noise source for this qubit), we achieve a Ramsey decay time T_2^* of 177 ns and a Rabi decay time $1/\Gamma_{\text{Rabi}}$ exceeding 1 μs . We find that the slowest Γ_{Rabi} is limited by fluctuations in the Rabi frequency induced by charge noise and not by fluctuations in the qubit energy itself.

INTRODUCTION

There has been much progress in the development of qubits in semiconductor quantum dots [1], making use of one [2–11], two [12–20], and three quantum dots [21–26] to host qubits. Charge noise is often the leading source of decoherence in semiconductor qubits [27], and an advantage of using two or more quantum dots to host a single qubit is the ability to work at sweet spots, a technique pioneered in superconducting qubits [28], that make the qubit more resistant to charge noise [29–36].

In this work we focus on one such qubit, the quantum dot hybrid qubit (QDHQ) [37–45], which is formed from three electrons in a double quantum dot, and can be viewed as a hybrid of a spin qubit and a charge qubit. Fast, full electrical control of the QDHQ was recently implemented experimentally using ac gating [46], demonstrating a free induction decay (FID) time of 11 ns through operation in the spin-like operating region (see Fig. 1). While QDHQ gating times are fast, substantial further improvements in QDHQ coherence times are required to achieve the high-fidelity gating necessary for fault-tolerant operation [47]. True sweet spots, which are used to increase resistance to noise and thus increase coherence, are defined by a zero derivative of the qubit energy with respect to a parameter subject to noise. Sweet spots are usually found at specific points of zero extent in parameter space, so that non-infinitesimal noise amplitude temporarily moves a qubit off the sweet spot. The spin-like regime of the QDHQ has no true sweet spot; however, it has a large and extended region of small $dE_Q/d\varepsilon$, where E_Q is the qubit energy and ε is the detuning between the two quantum dots.

Here we show that the spin-like operating regime for the QDHQ can be made resilient to charge noise by ap-

propriate tuning of the internal parameters of the qubit. By measuring $dE_Q/d\varepsilon$, we are able to identify dot tuning parameters that increase resiliency to charge noise. These measurements show that the three-electron QDHQ can be tuned *in-situ* in ways that have a predictable and understandable impact on the qubit coherence: the qubit dispersion can be tuned smoothly by varying device gate voltages, and we find that the dephasing rate is proportional to $dE_Q/d\varepsilon$, consistent with a charge noise dephasing mechanism. Reducing $dE_Q/d\varepsilon$ significantly enhances the coherence of the qubit. We have achieved an increase the coherence times by more than an order of magnitude over previous work, decreasing the Rabi decay rate Γ_{Rabi} from 67.1 MHz to 0.98 MHz, and increasing the FID time T_2^* to as long as 177 ns. These parameters correspond to an infidelity contribution from pure dephasing of about 1%.

RESULTS

Fig. 1 shows the energy levels of the QDHQ as a function of the detuning ε . At negative detuning the energy difference between the $|0\rangle$ and $|1\rangle$ states is dominated by the Coulomb energy, while at large positive detunings, where both logical states have the same electron configuration (one electron on the left and two on the right), the energy difference is dominated by the single-particle splitting E_R between the lowest two valley-orbit states in the right dot. Here the logical states are described by their spin configuration: $|0\rangle = |\downarrow\rangle|S\rangle$ and $|1\rangle = \sqrt{1/3}|\downarrow\rangle|T_0\rangle - \sqrt{2/3}|\uparrow\rangle|T_-\rangle$, where $|\downarrow\rangle$ and $|\uparrow\rangle$ represent the spin configuration of the single electron in the left quantum dot and $|S\rangle$, $|T_0\rangle$, and $|T_-\rangle$ represent the singlet (S) and triplet (T_0 , T_-) spin configurations of the two electrons in the right quantum dot. The tunnel coupling $\Delta_{1(2)}$ describes the anticrossings between the right dot ground (first excited) state and left dot ground state.

* Current address: Sandia National Laboratories, Albuquerque, NM 87185, USA.

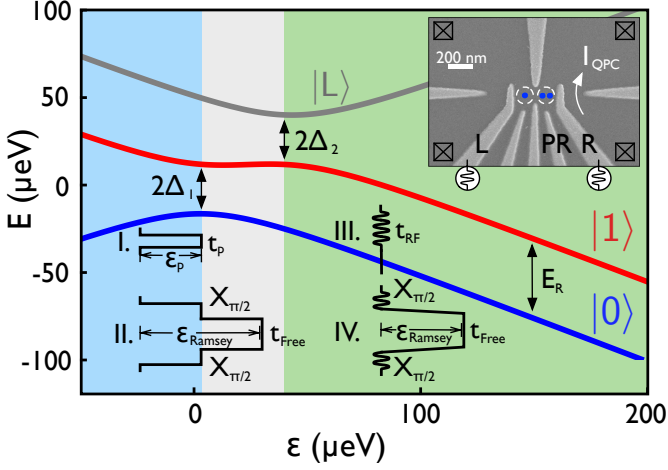


Figure 1. **Energy spectrum and pulse sequences for the quantum dot hybrid qubit (QDHQ).** Main panel: Energy versus detuning of the qubit states $|0\rangle$ and $|1\rangle$ as well as a leakage state $|L\rangle$. The QDHQ Hamiltonian, described in Supplementary Section 1, is parameterized using two tunnel couplings $\Delta_{1(2)}$ between the ground state of the left dot and the ground (excited) state of the right dot, and the asymptotic energy splitting E_R between the ground and excited states of the right dot. In the spin-like region (green, right), the logical states are differentiated by their spin configurations. The four pulse sequences used in this work are shown as functions of the detuning: the non-adiabatic Larmor (I) and Ramsey (II) sequences, and the microwave-pulsed Rabi (III) and Ramsey (IV) sequences. See Supplementary Section 4 for details. **Inset**, SEM image of a device lithographically identical to the one used in the experiments; white dashed circles indicate the locations of the double dot. Voltage pulses are applied to gates L and R, and a quantum point contact (QPC) is used to measure the electron occupancy of the dots.

Fig. 2a-g shows results of FID measurements for four different values of the measured $dE_Q/d\varepsilon$, performed using the pulse sequence of diagram IV of Fig. 1, in order to determine $\Gamma_2^* = 1/T_2^*$. For short times (panels a, c, e), Ramsey fringes are visible for all $dE_Q/d\varepsilon$; in contrast, for $t_{\text{Free}} = 22$ ns, Ramsey fringes are attenuated in Fig. 2b (large $dE_Q/d\varepsilon$), yet are still clearly visible in Fig. 2f (small $dE_Q/d\varepsilon$). As shown in Fig. 2g, by tuning the qubit to achieve $dE_Q/d\varepsilon = 0.0025$, Ramsey fringes are still visible at $t_{\text{Free}} = 120$ ns, and at this tuning a Gaussian fit to the Ramsey fringe amplitude (shown in Fig. 2h) yields $T_2^* = 177 \pm 9$ ns. Fits to the Ramsey fringe amplitude of the other three detunings are shown in Fig. 2i, demonstrating a strong correlation between small $dE_Q/d\varepsilon$ and long T_2^* . Although we have shown Gaussian fits in Fig. 2, consistent with quasistatic charge noise, we note that the FID decay also can be fit by an exponential decay, which would be consistent with noise that is dominated by only a few two-level fluctuators [48], and therefore we cannot distinguish between these two limiting cases (see supplemental material for fit parameters extracted from exponential decays).

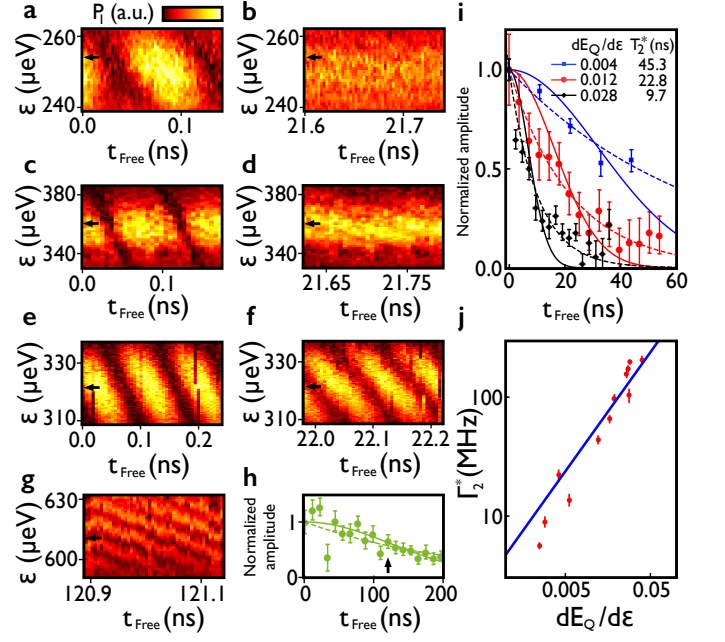


Figure 2. **Changing the dot tuning and ε to achieve small $dE_Q/d\varepsilon$ decreases the free induction decay (FID) rate by more than an order of magnitude.** **a-g** Plots showing the probability P_1 of being in state $|1\rangle$ after applying the Ramsey pulse sequence of diagram IV in Fig. 1, for qubit tunings characterized by different $dE_Q/d\varepsilon$ values. Two t_{Free} time windows are shown for three tunings, corresponding to $dE_Q/d\varepsilon=0.028$ (**a,b**), $dE_Q/d\varepsilon=0.012$ (**c,d**), $dE_Q/d\varepsilon=0.0042$ (**e,f**), and a single time window is shown for $dE_Q/d\varepsilon=0.0025$ (**g**). Comparing **b**, **d**, **f**, and **g**, we see that the FID rate decreases as $dE_Q/d\varepsilon$ decreases. **h**, **i**, Oscillation amplitudes as a function of t_{Free} , normalized by their value at $t_{\text{Free}} = 0$ are obtained at the ε values indicated by black arrows in **g** (**h**) and **a-f** (**i**); fits to both $\exp(-t_{\text{Free}}/T_2^*)$ (values shown) and $\exp(-t_{\text{Free}}^2/T_2^{*2})$ are plotted. **j**, Γ_2^* vs. $dE_Q/d\varepsilon$, obtained from a fit to $\exp(-t_{\text{Free}}/T_2^*)$, as in **i** (values extracted from a fit to $\exp(-t_{\text{Free}}/T_2^*)$ can be found in Supplementary Section 6), for several different tunings and a range of ε . The data are well fit to Eq. (1) (blue line, $\sigma_\varepsilon = 4.39 \pm 0.32 \mu\text{eV}$), providing evidence that Γ_2^* is limited by charge noise.

Fig. 2j shows $\Gamma_2^* = 1/T_2^*$ for a wide range of $dE_Q/d\varepsilon$, demonstrating a significant improvement in coherence for reduced values of $dE_Q/d\varepsilon$. For a gaussian distribution of quasistatic fluctuations of the detuning parameter, with a standard deviation of σ_ε , one expects that [15, 27]

$$\Gamma_2^* = |dE_Q/d\varepsilon| \sigma_\varepsilon / \sqrt{2}\hbar. \quad (1)$$

In Fig. 2j, we observe such a linear relation between Γ_2^* and $dE_Q/d\varepsilon$, with a fitting constant $\sigma_\varepsilon = 4.39 \pm 0.32 \mu\text{eV}$.

We now turn to a discussion of the Rabi decay time, $1/\Gamma_{\text{Rabi}}$, and its dependence on the qubit dispersion $dE_Q/d\varepsilon$. Fig. 3a shows both E_Q and $dE_Q/d\varepsilon$ as a function of detuning, calculated using the measured tuning parameters for Figs. 3b-e (see Supplementary Section 1 and 4), showing the decrease in the slope $dE_Q/d\varepsilon$ with

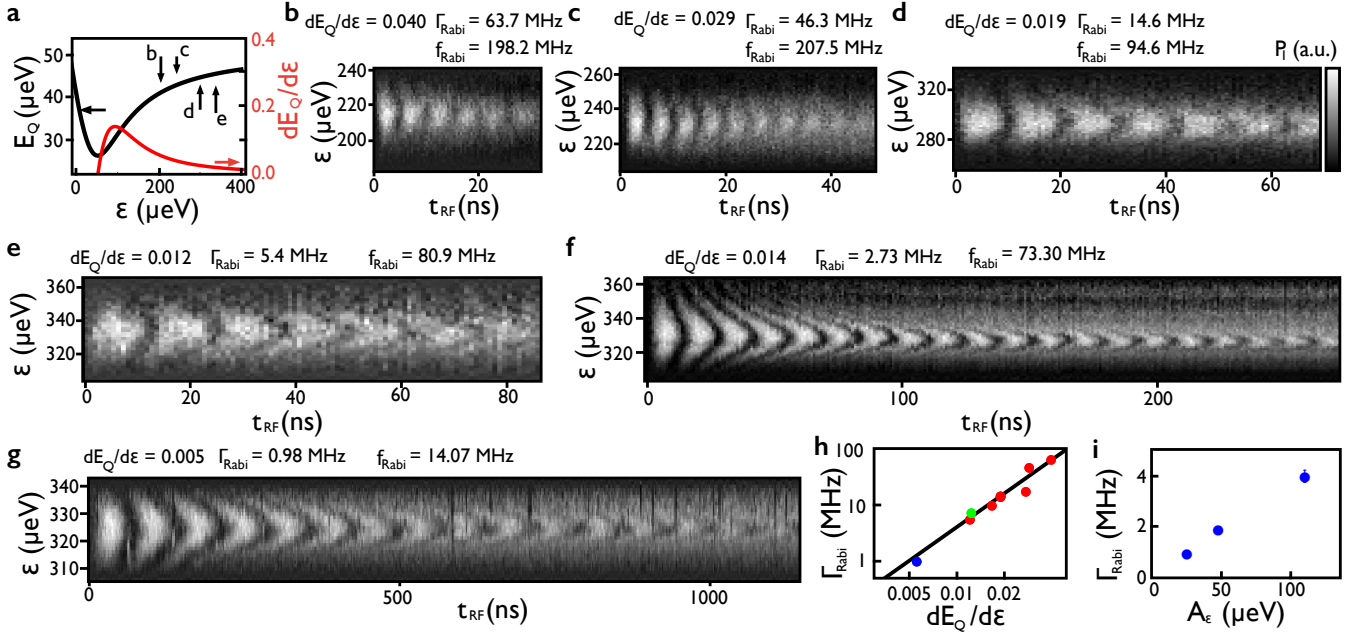


Figure 3. **Rabi decay rate is limited by charge noise and applied microwave power, A_ε .** **a**, Plots of $E_Q = hf_Q$ (black) and $dE_Q/d\varepsilon$ (red) versus ε for the tuning used in panels **b-e**. Here, f_Q is the qubit frequency, and the spectroscopy methods used are described in Supplementary Section 4. **b-e**, Rabi oscillations of the probability P_1 of being in state $|1\rangle$, all obtained at the same tuning but at different ε , ranging from ~ 210 to $340 \mu\text{eV}$. Γ_{Rabi} clearly decreases as $dE_Q/d\varepsilon$ decreases. The decrease in f_{Rabi} between panels **b-e** is caused by the decreased coupling to the left dot as ε is increased (see Eq. (2)). A_ε is nominally the same but changes slightly between panels **b-e** due to changes in f_Q as discussed in Supplementary Section 5. **f**, Rabi oscillations, taken at a different device tuning, demonstrating over 100 coherent $X_{\pi/2}$ rotations within a Rabi decay time. **g**, Rabi oscillations demonstrating a Rabi decay time longer than $1 \mu\text{s}$, taken at a device tuning differing from those in **b-f**. **h**, Γ_{Rabi} , obtained by fitting to an exponential decay, plotted as a function of $dE_Q/d\varepsilon$ for measurements at multiple tunings and operating points, with A_ε within 10% of $25 \mu\text{eV}$. Here, the black line has slope 2, indicating that Γ_{Rabi} depends quadratically on $dE_Q/d\varepsilon$, consistent with Γ_{Rabi} being limited by fluctuations of f_Q [48, 50]. Here, the different tunings are labeled with different colors (red, green, and blue), as specified in Supplementary Section 1. **i**, Rabi oscillations taken at $\varepsilon = 323 \mu\text{eV}$ ($dE_Q/d\varepsilon = 0.005$), as a function of the microwave amplitude A_ε , showing that the Rabi decay rate $\Gamma_{Rabi} \propto A_\varepsilon$, consistent with Γ_{Rabi} being limited by fluctuations of f_{Rabi} for small values of $dE_Q/d\varepsilon$.

increasing ε . Figs. 3b-e show Rabi oscillation measurements, performed with a microwave burst of duration t_{RF} and acquired at the detunings labeled b-e in Fig. 3a, showing that with increasing ε (and therefore decreasing $dE_Q/d\varepsilon$) the Rabi decay rate Γ_{Rabi} decreases by more than an order of magnitude for the data reported here.

For quantum gates, the contribution to infidelity arising from qubit decoherence is minimized when the ratio of the gate duration to the Rabi decay time is minimized. The data in Fig. 3f, acquired at a different dot tuning, shows that this ratio can be made small enough that an $X_{\pi/2}$ gate can be performed over 100 times within one Rabi decay time. In the absence of any other nonideality in the experiment, this would limit the fidelity of an $X_{\pi/2}$ rotation on the Bloch sphere to 99.0% and would represent a sevenfold improvement over previous results [46].

It is also interesting to consider how long the Rabi decay time, $1/\Gamma_{Rabi}$, itself can be. Fig. 3g shows Rabi oscillations acquired at a different dot tuning and a very small $dE_Q/d\varepsilon = 0.005$. Here, $\Gamma_{Rabi} = 0.98$ MHz, representing a decrease by more than a factor of 30 from

previously reported Rabi decay rates [46].

The decay of Rabi oscillations is caused by at least two different mechanisms [49], both of which are observed in these experiments. First, for relatively large values of $dE_Q/d\varepsilon$, fluctuations in E_Q from charge noise dominate the decoherence. This is similar to FID measurements, with the important difference that the microwave drive effectively reduces the range of frequencies decohering the qubit. This results in Rabi decoherence rates Γ_{Rabi} that are slower than the FID rates Γ_2^* at the same $dE_Q/d\varepsilon$. For this mechanism, the Rabi decay is expected to be exponential and depend quadratically on $dE_Q/d\varepsilon$ [48, 50]. Fig. 3h shows Γ_{Rabi} vs. $dE_Q/d\varepsilon$ and a quadratic fit to the data; the data are well-described by this functional form, and decreasing $dE_Q/d\varepsilon$ yields nearly two orders of magnitude decrease in Γ_{Rabi} .

Second, charge noise can also cause fluctuations in the rotation rate f_{Rabi} itself [49], and as $dE_Q/d\varepsilon$ becomes small, these fluctuations become the dominant source of decoherence. This second decay process is expected to yield a decay rate proportional to the drive amplitude

A_ε , and as shown in Fig. 3i, we observe this proportionality in the experiment for small $dE_Q/d\varepsilon$. Thus, for small $dE_Q/d\varepsilon$, fluctuations in f_{Rabi} dominate the Rabi decay rate. In contrast to the Rabi decay process discussed above, in which the applied microwave pulse narrows the frequency range of charge fluctuations contributing to the decay, charge fluctuations over a wide bandwidth are expected to contribute to this decay process. This contribution can be seen by applying the rotating wave approximation to Eq. (S1) in Supplementary Section 1, which yields an approximate form for f_{Rabi} that is valid at large detunings:

$$f_{\text{Rabi}} = \frac{\Delta_1 \Delta_2}{2h\varepsilon(\varepsilon - E_R)} A_\varepsilon. \quad (2)$$

σ_ε can then be related to σ_{Rabi} , the standard deviation of fluctuations in f_{Rabi} , by

$$\sigma_{\text{Rabi}} = (df_{\text{Rabi}}/d\varepsilon)\sigma_\varepsilon. \quad (3)$$

We therefore expect the decay rate from this mechanism to be proportional to $dE_Q/d\varepsilon$ rather than to the square of $dE_Q/d\varepsilon$, explaining its dominance at small $dE_Q/d\varepsilon$.

DISCUSSION

In this work we have shown that the internal parameters of the QDHQ can alter the qubit dispersion $dE_Q/d\varepsilon$ over a wide range, resulting in large tunability in both the decoherence rates and the Rabi frequencies achievable. The dominant dephasing mechanism for Rabi oscillations switches from fluctuations in the qubit energy E_Q to fluctuations in the Rabi frequency f_{Rabi} at the smallest values of $dE_Q/d\varepsilon$. By decreasing $dE_Q/d\varepsilon$ we have reduced both the Rabi and the Ramsey decoherence rates, important metrics for achieving high-fidelity quantum gate operations, by more than an order of magnitude compared with previous work, demonstrating Γ_{Rabi} as small as 0.98 MHz and $T_2^* = 1/\Gamma_2^*$ as long as 127 ns. These coherence times exhibit the utility of the extended near-sweet spot in the QDHQ for improving qubit performance in the presence of charge noise.

METHODS

The Si/SiGe device is operated in a region where magnetospectroscopy measurements [3, 51] have indicated that the valence electron occupation of the double dot is (1,2) for the qubit states studied here. Manipulation pulse sequences were generated using Tektronix 70001A arbitrary waveform generators and added to DC gate voltages on gates L and R using bias tees (PSPL5546). Because of the frequency dependent attenuation of the bias tees, corrections were made to the applied pulses during the adiabatic detuning pulses, as described in Supplementary Section 5. The qubit states were

mapped to the (1,1) and (1,2) charge occupation states as described in ref. [46]. A description of the methods used to measure the qubit dispersion and lever arm can be found in Supplementary Section 4.

Correspondence and requests for materials should be addressed to Mark A. Eriksson (maeriksson@wisc.edu)

ACKNOWLEDGEMENTS

This work was supported in part by ARO (W911NF-12-0607, W911NF-08-1-0482), NSF (DMR-1206915, PHY-1104660, DGE-1256259), and the Vannevar Bush Faculty Fellowship program sponsored by the Basic Research Office of the Assistant Secretary of Defense for Research and Engineering and funded by the Office of Naval Research through grant N00014-15-1-0029. Development and maintenance of the growth facilities used for fabricating samples is supported by DOE (DE-FG02-03ER46028). This research utilized NSF-supported shared facilities at the University of Wisconsin-Madison.

SUPPLEMENTAL MATERIAL FOR 'EXTENDING THE COHERENCE OF A QUANTUM DOT HYBRID QUBIT'

These supplemental materials present additional details of the experimental methods used.

S1. HAMILTONIAN OF THE QUANTUM DOT HYBRID QUBIT

The Hamiltonian of the quantum dot hybrid qubit (QDHQ) can be written as

$$\begin{pmatrix} \varepsilon/2 & \Delta_1 & -\Delta_2 \\ \Delta_1 & -\varepsilon/2 & 0 \\ -\Delta_2 & 0 & -\varepsilon/2 + E_R \end{pmatrix}. \quad (4)$$

If the tunnel couplings are assumed to be independent of ε , then Δ_1 , Δ_2 and E_R can be determined by fitting the spectrum obtained from Eq. (4) to the measured energy difference between the two lowest states of the QDHQ, $E_Q(\varepsilon)$. Table I shows the values of Δ_1 , Δ_2 and E_R obtained in this way for the 7 different dot tunings used in this experiment, as described below. The data in Figs. 2(a)-(b) is obtained at tuning 4, the data in Figs. 2(c)-(d) is obtained at tuning 1 while the data in Figs. 2(e)-(h) is obtained at tuning 3. For the data in Figs. 2(a)-(f) we used microwave pulsed Ramsey sequences with $\varepsilon_{\text{Ramsey}} = 0 \mu\text{eV}$ while in Figs. 2(e)-(h) $\varepsilon_{\text{Ramsey}} = 288.6 \mu\text{eV}$. The data in Figs. 3(b)-(e) are obtained at tuning 1, The data in Fig. 3(f) is obtained at tuning 7 while the data in Figs. 3(g) and (i) are acquired at tuning 3. In Fig. 3(h) red points are taken at tuning 1,

the green point at tuning 2 and the blue point at tuning 3, here A_ε was kept within 10% of $25 \mu\text{eV}$, as described in Sec. S5. For both Rabi and Ramsey measurements we use the measured energy spectrum to determine the resonant detuning value, ε , corresponding to the microwave frequency, $f_{\mu\text{w}}$, used in the experiments.

Tuning	Method	Δ_1 (μeV)	Δ_2 (μeV)	E_R (μeV)
1	I	18.1 ± 1.1	46.7 ± 3.1	51.7
2	IV	18.0 ± 5.9	49.0 ± 11.9	53.6 ± 9.4
3	IV	16.1 ± 1.7	35.5 ± 4.2	50.6 ± 3.7
4	I	16.9 ± 2.4	41.1 ± 3.4	49.6 ± 2.7
5	II	21.1 ± 2.6	67.3 ± 5.3	58.6 ± 5.3
6	IV	15.5 ± 1.3	33.4 ± 3.7	50.6 ± 2.7
7	IV	17.3 ± 0.8	50.2 ± 1.3	52.0

Table I. Values of Δ_1 , Δ_2 and E_R for each of the tunings used in this experiment. ‘Method’ refers to the Larmor or Ramsey pulse sequences indicated schematically in Fig. 1 of the main text.

S2. EXPERIMENTAL SETUP

The experiments were performed in a device with a gate design identical to the one shown in Fig. 1 of the main text, which was placed in a dilution refrigerator with a base temperature ≤ 30 mK. The electron temperature is estimated to be 143 ± 10 mK. [3]. The device was operated near the (2,1)-(1,2) charge transition. Here, (n, m) refers to a charge occupation of n electrons in the left dot and m electrons in the right dot, modulo a possible closed shell of electrons in one or both dots. All pulse sequences were generated using a Tektronix AWG70001A arbitrary waveform generator (AWG). Manipulations using non-adiabatic pulse sequences were performed by applying pulses while detuned to the charge-like (CL) region, highlighted blue (left part) in Fig. 1, where we initialize to a (2,1) charge occupation. In the charge-like region the two logical states have different charge configurations and are well described by $|0\rangle_{\text{CL}} = |L\rangle$ and $|1\rangle_{\text{CL}} = |R\rangle$, where state L (R) corresponds to two electrons in the left (right) quantum dot and one electron in the right (left) quantum dot. This enables readout by projecting the $|0\rangle_{\text{CL}}$ state onto (2,1) and the $|1\rangle_{\text{CL}}$ state onto (1,2). Manipulations using microwave pulse sequences were performed by applying microwaves while detuned to the spin-like (SL) region, highlighted green (right part) in Fig. 1, where the initial charge occupation is (1,2). To perform readout, spin-to-charge conversion is implemented near the (1,1) to (1,2) charge transition line, projecting the $|1\rangle_{\text{SL}}$ state onto a (1,1) charge configuration and the $|0\rangle_{\text{SL}}$ onto a (1,2) charge configuration. We measure the qubit charge configuration using the methods described in Ref. [46].

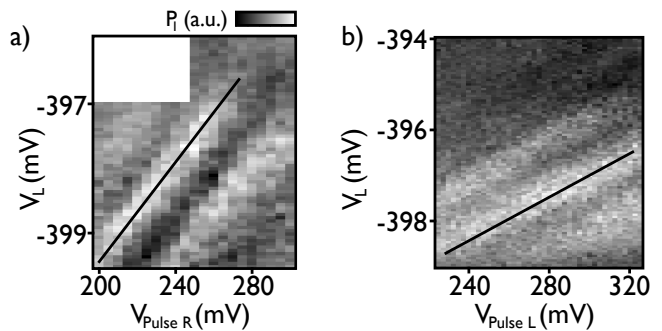


Figure 4. **Calibrating the amplitudes of high-frequency pulses on the L and R gates to dc voltage changes on the L gate.** **a**, The probability of being in the qubit state $|1\rangle$ after applying a 1 ns Larmor pulse (shown in diagram I of Fig. 1), resulting in Larmor oscillations as a function of the ac pulse amplitude on the R gate, $V_{\text{Pulse R}}$, and the dc voltage bias applied to gate L, V_L . The black line identifies one of the Larmor peaks. In this case, a change of the Larmor pulse amplitude of $\delta V_{\text{Pulse R}} = 28.8$ mV, corresponds to a shift in the dc bias on the L gate by $\delta V_L = 1.0$ mV. **b**, Analogous result when the Larmor pulse is applied to gate L. In this case, a change of the Larmor pulse amplitude by $\delta V_{\text{Pulse L}} = 47.4$ mV, corresponds to a shift in the dc bias on the L gate by $\delta V_L = 1.0$ mV.

S3. CALIBRATION OF PULSE AMPLITUDES TO GATE BIASES

The L and R gates can be used to apply high-frequency pulses, including non-adiabatic and microwave-driven pulses. (For simplicity here, we refer to both of these as ac pulses.) The electrostatic coupling between the gates and the dots is the same for any type of pulse. However, ac pulses are intentionally attenuated in our control circuitry, which effectively suppresses the ac lever arm. We can calibrate changes in the amplitude of applied pulses to changes in applied bias on the L gate by applying a 1 ns Larmor pulse to the L(R) gate and sweeping the bias of the L gate over the (2,1)-(1,2) charge polarization line. As the bias is swept, Larmor oscillations cause oscillations in the QPC current. Changing the amplitude of the pulse from $V_{\text{pulse L(R)}} = 225$ (200) mV to 325 (300) mV causes a shift in the position of the Larmor oscillation with respect to bias on the L gate, as shown in Fig. 4. For a $\delta V_{\text{pulse L(R)}} = 47.4$ (28.8) mV change in pulse amplitude applied to the L(R) gate the shift was measured to be a $\delta V_L = 1.0$ mV bias change on the L gate, yielding an effective ratio of pulse amplitudes to gate bias of

$$\frac{\delta V_L}{\delta V_{\text{pulse L(R)}}} = 0.021 \text{ (0.035)}. \quad (5)$$

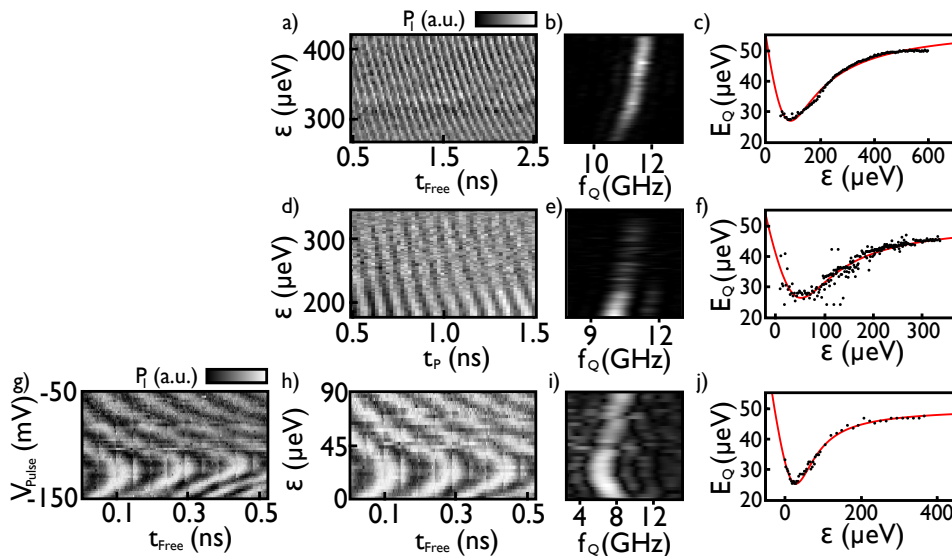


Figure 5. **Qubit spectroscopy measurements, using three different methods.** **a-c**, The non-adiabatic Ramsey pulse method, shown schematically in diagram II of Fig. 1 in the main text. **a**, The gray-scale image shows the probability of being in qubit state $|1\rangle$ as a function of the wait time, t_{Free} , and the detuning, $\varepsilon = \varepsilon_0 + \varepsilon_{\text{Ramsey}}$, where free induction occurs. Here, the base detuning, ε_0 , is swept from -290 to -175 μeV , while the pulse amplitude $\varepsilon_{\text{Ramsey}} = 505$ μeV remains constant for the whole scan. **b**, A time Fourier transform of the Ramsey oscillations in (a); the qubit frequency, f_Q , is identified as the location of the peak in the Fourier transform as a function of ε . **c**, $E_Q = hf_Q$ vs. ε , obtained by combining different Ramsey fringe measurements at tuning 5, with $\varepsilon_{\text{Ramsey}}$ in the range of 100-640 μeV . The red curve shows a fit to the QDHQ energy splitting, modelled in Eq. (4), assuming constant tunnel couplings; the resulting fitting parameters for tuning 5 are listed in Table I. **d-f**, The non-adiabatic Larmor pulse method, shown schematically in diagram I of Fig. 1. **d**, The gray-scale image shows the probability of being in qubit state $|1\rangle$ as a function of wait time, t_p , and the detuning, $\varepsilon = \varepsilon_0 + \varepsilon_p$, where the Larmor rotation is performed. In this case, the base detuning ε_0 is swept from -213 to -91 μeV , while $\varepsilon_p = 350$ μeV is held constant. **e**, A time Fourier transform of the data in (d), with the qubit frequency again identified as the location of the peak. **f**, E_Q vs. ε obtained by combining different Larmor fringe measurements at tuning 1, corresponding to ε_p in the range of 175-350 μeV . The red curve shows a fit to the model of Eq. (4), with constant tunnel couplings, yielding the results for tuning 1 listed in Table I. **g-j**, The microwave-driven Ramsey pulse method, shown schematically in diagram IV of Fig. 1. **g**, The gray-scale image shows the probability of being in qubit state $|1\rangle$ as a function of wait time, t_{Free} , and the uncalibrated pulse amplitude of the adiabatic pulse, V_{Pulse} , where the free induction occurs. Here, the base detuning is kept constant at $\varepsilon_0 = 210$ μeV , while V_{Pulse} is swept from -150 to -100 mV. **h**, The same data as (g), replotted as a function of $\varepsilon = \varepsilon_0 + \varepsilon_{\text{Ramsey}}$. In this case, V_{Pulse} has been scaled to take into account the frequency-dependent attenuation in the circuit between the arbitrary waveform generator and the sample, which distorts the pulse shape at short times, (see Sec. S5.) and then scaled to $\varepsilon_{\text{Ramsey}}$ using $\alpha_{\varepsilon, R}^{\text{ac}}$ (see Sec. S4). **i**, A time Fourier transform of the data in (h), with the qubit frequency identified as the location of the peak. **j**, E_Q vs. ε obtained by combining different microwave-driven Ramsey fringe measurements at tuning 3. The red curve shows a fit to the model of Eq. (4), with constant tunnel couplings, yielding the results for tuning 3 listed in Table I.

S4. MEASURING THE QUBIT ENERGY SPECTRUM AND DETERMINING THE LEVER ARMS

The energy difference between the two qubit states was measured as a function of detuning using three different techniques: non-adiabatic Larmor and Ramsey pulse sequences, corresponding to diagrams I and II in Fig. 1 of the main text, and a microwave-pulsed Ramsey sequence corresponding to diagram IV.

For the microwave pulsed Ramsey sequence, initialization and readout are performed in the spin-like regime at the base detuning ε_0 , using state-dependent tunneling between the charge configurations (1, 1) and (1, 2), as described in Sec. S2 and Ref. [46]. First we perform an $X_{\pi/2}$ rotation at $\varepsilon = \varepsilon_0$. The microwave driv-

ing frequency is set to the qubit resonant frequency $f_{\mu w} = f_Q(\varepsilon_0) = E_Q(\varepsilon_0)/h$, and the pulse duration ranges from 1.2 to 17.7 ns, depending on the tuning of the device. These microwave pulses are turned on and off smoothly over 200 ps, time periods that are included in the total pulse duration. After the first microwave burst we adiabatically, over a 400 ps time period, change the detuning to $\varepsilon = \varepsilon_0 + \varepsilon_{\text{Ramsey}}$ as shown in diagram IV in Fig. 1 of the main text, so that the probabilities of the logical states are unaffected. Phase is accumulated between the logical states during the wait time t_{Free} , after which the detuning is adiabatically changed back to $\varepsilon = \varepsilon_0$, again over a 400 ps time period, before performing a second microwave-driven $X_{\pi/2}$ rotation. This procedure yields Ramsey oscillations as a function of the wait time, t_{Free} , with a frequency given by $E_Q(\varepsilon_0 + \varepsilon_{\text{Ramsey}})/h$. Hence, by measuring the Ramsey oscillation frequency, we can de-

termine the qubit energy, E_Q . By varying ε_0 or $\varepsilon_{\text{Ramsey}}$, the energy spectrum can be mapped out over a wide range of detuning values. The microwave method was employed at tunings 2, 3 [Figs. 5(g)-(j)], 6 and 7 to obtain the corresponding energy spectra. Fitting the data to Eq. (4) yields the results shown in Table I. The lever arm $\alpha_{\varepsilon,L}$ was determined by replacing ε in Eq. (4) with $\alpha_{\varepsilon,L}(V_L - V_{L,0})$, where $V_{L,0}$ is the V_L bias corresponding to $\varepsilon = 0$ μeV , and fitting for $\alpha_{\varepsilon,L}$. The quality of this fit increases as more points are acquired at negative ε values where $dE_Q/d\varepsilon \rightarrow -1$. The greatest number of points in this regime were acquired at tuning 6, where a fit yielded

$$\alpha_{\varepsilon,L} = 41.36 \mu\text{eV}/\text{mV}. \quad (6)$$

We then calculate the lever arm between detuning and ac pulses:

$$\alpha_{\varepsilon,L(R)}^{\text{ac}} = \alpha_{\varepsilon,L} \frac{\delta V_L}{\delta V_{\text{pulse L(R)}}} = 0.87 (1.46) \mu\text{eV}/\text{mV}. \quad (7)$$

The microwave driving method was also used to obtain the data in Figs. 2 and 3 of the main text. When using the method to determine the FID rate, Γ_2^* , it is inconvenient to increase t_{Free} to large times, $> T_2^*$, because the decoherence rate in the spin-like region is very slow compared to the qubit frequency, and measuring for both long times and with short time steps is prohibitively time-consuming. Instead, we obtain a series of widely separated time windows, with good resolution in each window. These windows range in size from 120 to 400 ps, encompassing 1.5-6 oscillations, and the separation between the windows is 0.6 – 22.0 ns, getting larger as Γ_2^* decreases. A given Γ_2^* measurement includes at least 5 such windows.

For the non-adiabatic Ramsey pulse sequence shown schematically in diagram II of Fig. 1, the qubit begins in its ground state at a base detuning value of $\varepsilon_0 \ll 0$ in the charge-like region. We then pulse the detuning to the avoided crossing at $\varepsilon = 0$, where the energy eigenstates are $|0\rangle_{\varepsilon=0} = (|0\rangle_{\text{CL}} - |1\rangle_{\text{CL}})/\sqrt{2}$ and $|1\rangle_{\varepsilon=0} = (|0\rangle_{\text{CL}} + |1\rangle_{\text{CL}})/\sqrt{2}$. Waiting at this position for a time t_p yields an $X_{5\pi/2}$ rotation in the original basis, such that the qubit is in state $|-Y\rangle_{\text{CL}} = (|0\rangle_{\text{CL}} - i|1\rangle_{\text{CL}})/\sqrt{2}$. We note that a $5\pi/2$ rotation was used here, instead of a $\pi/2$ rotation, because the 20 ps time resolution of our AWG allows us to better match the period of a $5\pi/2$ rotation than a $\pi/2$ rotation. We then pulse to another detuning value, $\varepsilon_0 + \varepsilon_{\text{Ramsey}}$, and wait for a time t_{Free} . This results in a phase accumulation of $\psi = e^{-it_{\text{Free}}E_Q(\varepsilon_0 + \varepsilon_{\text{Ramsey}})/\hbar}$ between the logical states, $|0\rangle_{\varepsilon_0 + \varepsilon_{\text{Ramsey}}}$ and $|1\rangle_{\varepsilon_0 + \varepsilon_{\text{Ramsey}}}$. We then pulse back to the avoided crossing, $\varepsilon = 0$, and perform another $X_{5\pi/2}$ rotation. Finally we pulse back to the base detuning, ε_0 , and readout the qubit by measuring its charge configuration. Similar to the microwave pulsed Ramsey method, the microwave-driven sequence yields oscillations as a function of the wait time t_{Free} , with frequency $E_Q(\varepsilon_0 + \varepsilon_{\text{Ramsey}})/\hbar$. This method was used in Figs. 5(a)-(c) to determine the qubit energy spectrum at

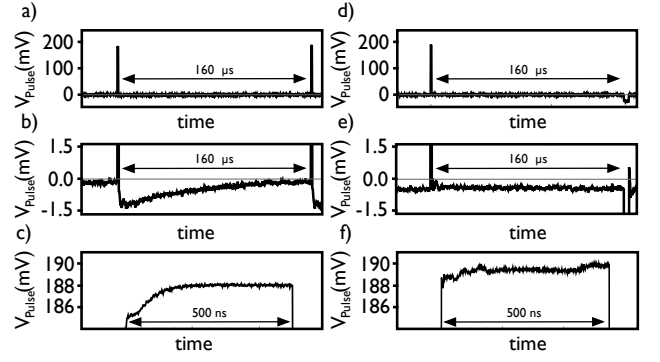


Figure 6. **Scope traces of an adiabatic pulse before and after pulse corrections.** **a**, A 500 ns adiabatic pulse with a 0.5 ns in and out adiabatic ramps after passing through a bias-tee. The pulse is repeated every 160 μs . **b**, Zoomed-in image of the bottom of the pulse in **(a)** showing distortions due to frequency-dependent attenuation. **c**, Zoomed-in image of the top of the pulse in **(a)**, showing distortions due to frequency-dependent attenuation. The behavior of both the top and bottom parts was fitted by subtracting multiple exponential decays of different amplitudes and time constants from the desired pulse shape, Eq. (8). **d**, A 500 ns adiabatic pulse with a 0.5 ns in and out adiabatic ramps and pulse corrections applied that compensate for the frequency-dependent attenuation. Here, instead of repeating the pulse every 160 μs , we interleave a pulse with lower opposite amplitude but equal area between measurement pulses to reduce the dc offset. The pulse corrections, in this case, have the same time constants and relative amplitudes obtained by fitting the uncorrected pulse. **e**, Zoomed-in image of the bottom of the corrected pulse shown in **(d)**. **f**, Zoomed-in image of the top of the corrected pulse shown in **(d)**.

tuning 5. Fitting the results to Eq. (4) yields the fitting parameters shown in Table I.

Finally, the non-adiabatic Larmor pulse sequence is shown schematically in diagram I of Fig. 1. It involves pulsing the detuning from its base value, $\varepsilon_0 \ll 0$, to the position $\varepsilon_0 + \varepsilon_p$. After waiting for a time t_p , the logical states of the qubit, $|0\rangle_{\varepsilon_0 + \varepsilon_p}$ and $|1\rangle_{\varepsilon_0 + \varepsilon_p}$, accumulate a phase difference of $\phi = e^{-it_p E_Q(\varepsilon_0 + \varepsilon_p)/\hbar}$, where $E_Q(\varepsilon_0 + \varepsilon_p)$ is the qubit energy splitting at $\varepsilon = \varepsilon_0 + \varepsilon_p$. Readout is then performed by pulsing back to ε_0 and measuring the charge configuration. By varying ε_0 and ε_p , the qubit energy spectrum can again be measured over a wide range of detuning values. This method was employed at tunings 1 [Figs. 5(d)-(f)] and 4 to obtain the corresponding energy spectra. Fitting these data to Eq. (4) yields the results shown in Table I.

S5. METHODS FOR CORRECTING DISTORTIONS IN HIGH FREQUENCY PULSE SEQUENCES

An arbitrary waveform generator (AWG) allows for the creation and application of complex pulse sequences.

Frequency-dependent attenuation caused by non-ideal RF-components of the experimental apparatus can cause distortions in the pulse shape before reaching the sample. Such is the case with the long adiabatic pulses used to measure the FID rate at the highest measured detunings. Here, the bandwidth between the AWG and the sample is limited by a bias-tee (PSPL5546) located in the coldest stage of the refrigerator (≤ 30 mK) with a bandwidth from 3.5 KHz to 7 GHz. To compensate for this bandwidth limitation we applied a long adiabatic pulse through an identical bias-tee at room temperature and measured its shape using an oscilloscope (Tektronix DPO72504D), and then applied corrections to the generated pulse until the desired pulse shape was displayed on the oscilloscope. Figs. 6(a)-(c) show the shape of an uncorrected pulse after passing through a bias-tee. To compensate for the consistent dc offset seen in Fig. 6(b) we interleave a second pulse that has the same area (pulse length \times pulse amplitude) and period as the measurement pulse but opposite amplitude. We also find that adding an offset ($A_{b,\text{off}}$) after the measurement pulse but not after the interleaved pulse further reduces the dc offset. To compensate for the shape distortions we fitted 4 different exponential decays with different amplitudes $A_{t(b),i}$ and time constants $\tau_{t(b),i}$ to the difference of the measured pulse top (bottom) to that of the target pulse. All these corrections can be specified using 17 different parameters that are listed in Table. II.

Correction (i)	$\tau_{t(b),i}$ (ns)	$A_{t(b),i}$	Scaling of $A_{t(b),i}$ (mV)
t,1	1.25	19.5	Amplitude
t,2	5.00	-2.0	Amplitude
t,3	30.0	-0.8	Amplitude
t,4	120	4.0	Amplitude
b,1	1.25	-17.5	Area
b,2	5.00	2.0	Area
b,3	80.0	-3.0	Area
b,4	1560	1.5	Area
off	-	2.5	Area

Table II. Pulse correction amplitudes and time constants for a 500 ns pulse with 200 mV amplitude and a period of 160 μ s and a interleaved 4000 ns pulse with -25 mV amplitude and a period of 160 μ s. We find that some correction amplitudes scale with the pulse amplitude while others scale with both the pulse amplitude and duration (pulse area). We find that the time constants are independent of both pulse amplitude and pulse duration.

The correction is then applied by adding

$$\sum_{i=1}^4 A_{t(b),i} \exp(-t/\tau_{t(b),i}) \quad (8)$$

to the top (bottom) segment of the pulse and adding $A_{b,\text{off}}$ after the first pulse. Figs. 6(d)-(f) show the shape of a corrected pulse after passing through the bias-tee. In principle, the corrections can be improved by repeating this process, but in practice, further improvements are limited by the vertical resolution of the AWG (0.5 mV). Due to the frequency dependent attenuation the microwave amplitude, A_ε at the sample changes as $f_{\mu w}$ is changed. This was corrected for by measuring A_ε at each $f_{\mu w}$ used after passing a microwave through the room temperature bias-tee and adjusting A_ε until it was within 10% of $A_\varepsilon = 25 \mu\text{eV}$.

S6. VALUES OF T_2^* EXTRACTED FROM FID DATA

$dE/d\varepsilon$	$T_{2,\text{Gaussian}}^*$ (ns)	$T_{2,\text{Exp}}^*$ (ns)
0.0399	5.0 ± 0.3	5.3 ± 0.3
0.0289	5.1 ± 0.2	4.7 ± 0.3
0.0283	9.7 ± 1.2	10.1 ± 0.7
0.0275	5.8 ± 0.3	6.3 ± 0.6
0.0265	6.4 ± 0.4	6.2 ± 0.4
0.0190	10.4 ± 0.8	17.4 ± 2.6
0.0167	15.4 ± 1.0	19.2 ± 3.0
0.0122	22.8 ± 1.6	22.1 ± 1.1
0.0056	73.1 ± 7.8	67.6 ± 4.2
0.0042	45.3 ± 4.4	66.7 ± 5.6
0.0029	112 ± 10	136 ± 24
0.0025	177 ± 9	215 ± 23

Table III. Values of T_2^* for fits to both a Gaussian and an exponential decay as a function of $dE/d\varepsilon$. A fit to Eq. 1 of the main text yields $\sigma_\varepsilon = 4.42 \pm 0.44 \mu\text{eV}$ for the $T_{2,\text{Exp}}^*$ values and $\sigma_\varepsilon = 4.39 \pm 0.32 \mu\text{eV}$ for the $T_{2,\text{Gaussian}}^*$ values.

-
- [1] Loss, D. & DiVincenzo, D. P. Quantum computation with quantum dots. *Phys. Rev. A* **57**, 120–126 (1998).
- [2] Koppens, F. H. L. *et al.* Driven coherent oscillations of a single electron spin in a quantum dot. *Nature* **442**, 766–771 (2006).
- [3] Simmons, C. B. *et al.* Tunable spin loading and T_1 of a silicon spin qubit measured by single-shot readout. *Phys. Rev. Lett.* **106**, 156804 (2011).
- [4] Pla, J. J. *et al.* A single-atom electron spin qubit in silicon. *Nature* **489**, 541–545 (2012).
- [5] Veldhorst, M. *et al.* An addressable quantum dot qubit with fault-tolerant control-fidelity. *Nature Nanotech.* **9**, 981–985 (2014).
- [6] Kawakami, E. *et al.* Electrical control of a long-lived spin qubit in a Si/SiGe quantum dot. *Nature Nanotech.* **9**, 666–670 (2014).
- [7] Yoneda, J. *et al.* Fast Electrical Control of Single Electron Spins in Quantum Dots with Vanishing Influence from Nuclear Spins. *Physical Review Letters* **113**, 267601–5 (2014).
- [8] Veldhorst, M. *et al.* A two-qubit logic gate in silicon. *Nature* **526**, 410–414 (2015).
- [9] Scarlino, P. *et al.* Second-harmonic coherent driving of a spin qubit in a si/sige quantum dot. *Phys. Rev. Lett.* **115**, 106802 (2015).
- [10] House, M. G. *et al.* High-Sensitivity Charge Detection with a Single-Lead Quantum Dot for Scalable Quantum Computation. *Physical Review Applied* **6**, 044016–6 (2016).
- [11] Takeda, K. *et al.* A fault-tolerant addressable spin qubit in a natural silicon quantum dot. *Science Adv.* **2**, 1600694 (2016).
- [12] Levy, J. Universal quantum computation with spin-1/2 pairs and Heisenberg exchange. *Phys. Rev. Lett.* **89**, 147902 (2002).
- [13] Petta, J. R. *et al.* Coherent manipulation of coupled electron spins in semiconductor quantum dots. *Science* **309**, 2180–2184 (2005).
- [14] Foletti, S., Bluhm, H., Mahalu, D., Umansky, V. & Yacoby, A. Universal quantum control of two-electron spin quantum bits using dynamic nuclear polarization. *Nature Physics* **5**, 903–908 (2009).
- [15] Petersson, K. D., Petta, J. R., Lu, H. & Gossard, A. C. Quantum coherence in a one-electron semiconductor charge qubit. *Phys. Rev. Lett.* **105**, 246804 (2010).
- [16] Maune, B. M. *et al.* Coherent singlet-triplet oscillations in a silicon-based double quantum dot. *Nature* **481**, 344–347 (2012).
- [17] Wang, K., Payette, C., Dovzhenko, Y., Deelman, P. W. & Petta, J. R. Charge relaxation in a single-electron Si/SiGe double quantum dot. *Phys. Rev. Lett.* **111**, 046801 (2013).
- [18] Shi, Z. *et al.* Coherent quantum oscillations and echo measurements of a si charge qubit. *Phys. Rev. B* **88**, 075416 (2013).
- [19] Wu, X. *et al.* Two-axis control of singlet-triplet qubit with an integrated micromagnet. *Proc. Nat. Acad. Sci.* **111**, 11938 (2014).
- [20] Harvey-Collard, P. *et al.* Nuclear-driven electron spin rotations in a single donor coupled to a silicon quantum dot. *arXiv.org* (2015). arXiv:1512.01606v1.
- [21] DiVincenzo, D. P., Bacon, D., Kempe, J., Burkard, G. & Whaley, K. B. Universal quantum computation with the exchange interaction. *Nature* **408**, 339 (2000).
- [22] Laird, E. A. *et al.* Coherent spin manipulation in an exchange-only qubit. *Phys. Rev. B* **82**, 075403 (2010).
- [23] Gaudreau, L. *et al.* Coherent control of three-spin states in a triple quantum dot. *Nature Physics* **8**, 54–58 (2011).
- [24] Medford, J. *et al.* Self-consistent measurement and state tomography of an exchange-only spin qubit. *Nature Nanotech.* **8**, 654–659 (2013).
- [25] Eng, K. *et al.* Isotopically enhanced triple-quantum-dot qubit. *Science Adv.* **1**, 1500214 (2015).
- [26] Russ, M. & Burkard, G. Asymmetric resonant exchange qubit under the influence of electrical noise. *Phys. Rev. B* **91**, 235411 (2015).
- [27] Dial, O. E. *et al.* Charge noise spectroscopy using coherent exchange oscillations in a singlet-triplet qubit. *Phys. Rev. Lett.* **110**, 146804 (2013).
- [28] Vion, D. *et al.* Manipulating the quantum state of an electrical circuit. *Science* **296**, 886–889 (2002).
- [29] Taylor, J. M., Srinivasa, V. & Medford, J. Electrically Protected Resonant Exchange Qubits in Triple Quantum Dots. *Phys. Rev. Lett.* **111**, 050502 (2013).
- [30] Medford, J. *et al.* Quantum-dot-based resonant exchange qubit. *Phys. Rev. Lett.* **111**, 050501 (2013).
- [31] Kim, D. *et al.* Microwave-driven coherent operations of a semiconductor quantum dot charge qubit. *Nature Nano.* **10**, 243–247 (2015).
- [32] Fei, J. *et al.* Characterizing gate operations near the sweet spot of an exchange-only qubit. *Physical Review B* **91**, 205434 (2015).
- [33] Reed, M. *et al.* Reduced sensitivity to charge noise in semiconductor spin qubits via symmetric operation. *Phys. Rev. Lett.* **116**, 110402 (2016).
- [34] Martins, F. *et al.* Noise Suppression Using Symmetric Exchange Gates in Spin Qubits. *Phys. Rev. Lett.* **116**, 116801 (2016).
- [35] Shim, Y.-P. & Tahan, C. Charge-noise-insensitive gate operations for always-on, exchange-only qubits. *Phys. Rev. B* **93**, 121410 (2016).
- [36] Nichol, J. M. *et al.* High-fidelity entangling gate for double-quantum-dot spin qubits. *npj Quant. Inform.* **3**, 1–4 (2017).
- [37] Shi, Z. *et al.* Fast hybrid silicon double-quantum-dot qubit. *Phys. Rev. Lett.* **108**, 140503 (2012).
- [38] Koh, T. S., Coppersmith, S. N. & Friesen, M. High-fidelity gates in quantum dot spin qubits. *Proc. Nat. Acad. Sci.* **110**, 19695–19700 (2013).
- [39] Kim, D. *et al.* Quantum control and process tomography of a semiconductor quantum dot hybrid qubit. *Nature* **511**, 70–74 (2014).
- [40] Ferraro, E., De Michielis, M., Mazzeo, G., Fanciulli, M. & Prati, E. Effective hamiltonian for the hybrid double quantum dot qubit. *Quant. Inform. Process.* **13**, 1155–1173 (2014).
- [41] Mehl, S. Quantum computation with three-electron double quantum dots at an optimal operation point. *arXiv:1507.03425v1*.
- [42] De Michielis, M., Ferraro, E., Fanciulli, M. & Prati, E. Universal set of quantum gates for double-dot exchange-only spin qubits with intradot coupling. *J. Phys. A:*

- Math. and Theor.* **48**, 065304 (2015).
- [43] Cao, G. *et al.* Tunable Hybrid Qubit in a GaAs Double Quantum Dot. *Phys. Rev. Lett.* **116**, 086801 (2016).
- [44] Wong, C. H. High-fidelity ac gate operations of a three-electron double quantum dot qubit. *Phys. Rev. B* **93**, 035409 (2016).
- [45] Chen, B.-B. *et al.* Spin blockade and coherent dynamics of high-spin states in a three-electron double quantum dot. *Phys. Rev. B* **95**, 035408 (2017).
- [46] Kim, D. *et al.* High-fidelity resonant gating of a silicon-based quantum dot hybrid qubit. *npj Quant. Inform.* **1**, 15004 (2015).
- [47] Fowler, A. G., Mariantoni, M., Martinis, J. M. & Cleland, A. N. Surface codes: Towards practical large-scale quantum computation. *Phys. Rev. A* **86**, 032324 (2012).
- [48] Ithier, G. *et al.* Decoherence in a superconducting quantum bit circuit. *Phys. Rev. B* **72**, 134519 (2005).
- [49] Yan, F. *et al.* Rotating-frame relaxation as a noise spectrum analyser of a superconducting qubit undergoing driven evolution. *Nature Comm.* **4**, 2337 (2013).
- [50] Jing, J., Huang, P. & Hu, X. Decoherence of an electrically driven spin qubit. *Phys. Rev. A* **90**, 022118 (2014).
- [51] Shi, Z. *et al.* Tunable singlet-triplet splitting in a few-electron Si/SiGe quantum dot. *Appl. Phys. Lett.* **99**, 233108 (2011).